Next-to-leading-logarithm calculation of direct photon production

H. Baer, J. Ohnemus, and J. F. Owens
Department of Physics, B-159, Florida State University, Tallahassee, Florida 32306
(Received 20 February 1990)

A method for calculating the production of direct photons beyond the leading-logarithm approximation has been developed, utilizing a combination of analytic and Monte Carlo integration methods. The method is described and examples are given, including a comparison with experimental results for the inclusive single-photon invariant cross section and the photon-plus-jet cross section. The flexibility of the Monte Carlo technique makes it straightforward to calculate a variety of observables and to take into account experimental cuts while still retaining the next-to-leading-logarithm terms.

I. INTRODUCTION

The production of large-transverse-momentum photons has long been recognized as an excellent process for studying the dynamics of hard-scattering processes.[1,2] The advantages of studying such direct photons are both numerous and well known. Briefly, the process is simple. To first order only two subprocesses contribute: $gq \to \gamma q$ and $q\bar{q} \to \gamma g$. Experimentally, photons are easier to reconstruct in a detector than are jets. Theoretically, the photon's simple coupling makes it much easier to perform next-to-leading-order calculations which are necessary for precise tests of QCD. Finally, the dominance of the $gq \to \gamma q$ subprocess in many kinematical regions is useful for determining the gluon distribution within the proton.

This paper presents a Monte Carlo method for performing a next-to-leading-logarithm calculation of direct photon production.[3] Similar methods have been used to perform next-to-leading-logarithm calculations for the photoproduction[4] of jets. In order to illustrate the utility of this approach, results for the inclusive invariant cross section are compared to data taken at center-of-mass energies ranging from 23 GeV to 1.8 TeV. Results for the photon-plus-jet cross section are also presented and compared with existing data.

The leading-logarithm approximation lies at the heart of most hard-scattering calculations. One of the weak points in such a calculation is that one has only an order-of-magnitude estimate for the renormalization and factorization scales. Typically, these scales are expected to be of the order of the square of the hard-scattering momentum transfer, e.g., p_T^2, of the observed photon in a single-photon inclusive calculation. Variations in these quantities can lead to significant changes in the normalization and, to a lesser extent shapes, of the resulting predictions. Thus, predictions of absolute normalizations are subject to large theoretical uncertainties when the leading-logarithm approximation is used. Relative normalizations, however, are less subject to these uncertainties. Representative examples of such calculations are reviewed in Ref. 1.

In order to achieve a higher level of theoretical precision, it is necessary to go beyond the leading-logarithm approximation; one must at least include the next-to-leading logarithms.[5] In many instances such calculations show a less dramatic dependence on the renormalization and factorization scale choices than in the case where only the leading logarithms are used. However, retaining subleading logarithms leads, in general, to more complex calculations. Furthermore, it is often difficult to calculate the quantities which are observable in a given experiment, taking into account the acceptances of the detector, different jet definitions, etc. In addition, each new observable requires a new calculation. For this reason, we have utilized a Monte Carlo technique for performing the next-to-leading-logarithm calculations. This technique is straightforward to implement and does not require an inordinate amount of computer time. Furthermore, new observables can be calculated by simply modifying the histogrammed quantities. The additional theoretical expressions are neither long nor complicated.

The remainder of this paper is organized as follows. The basic techniques used in the Monte Carlo next-to-leading-logarithm calculation are presented in Sec. II. Section III contains a discussion of the results obtained using the techniques presented in the previous section and Sec. IV contains summary remarks. Finally, there is an appendix which contains the expressions used in the construction of the Monte Carlo program. A preliminary report of some of these results was given in Ref. 3.

II. MONTE CARLO FORMALISM

The basic Monte Carlo technique has been discussed in both Refs. 3 and 4. However, a brief review of both the motivation and the notation will be of use in understanding the applications to be discussed in the next section. The lowest-order subprocesses which give rise to high-p_T photons are the $O(\alpha\alpha_s)$ subprocesses $gq \to \gamma q$ and $q\bar{q} \to \gamma g$. The characteristic signature of both of these is that the photon is isolated from the other hadrons in the event and it recoils against a balancing high-p_T jet which

appears on the opposite side of the event. In a leading-logarithm calculation, the effects of higher-order processes show up via the use of the strong-running coupling and scale-violating parton distributions. These latter functions are calculated using collinear kinematics so that the underlying event structure is expected to be similar to that given by the lowest-order subprocesses. When the $O(\alpha\alpha_s^2)$ subprocesses are considered, the situation becomes more complex. There exist regions of phase space where the photon can be emitted collinear with a quark, coming from such subprocesses as $qq \to qq\gamma$. Here the photon will be accompanied by hadrons fragmenting from the collinear quark so that it is no longer isolated. Such contributions collectively constitute the bremsstrahlung component of the photon signal. In an inclusive calculation, the unobserved quanta are integrated over. In the case of the bremsstrahlung contributions the integration over the angle between the photon and the quark from which it was emitted builds up a logarithm whose argument is of the order of the transverse momentum of the photon. Since the bremsstrahlung photons are emitted predominantly along the direction of motion of the parent parton, it is convenient to define a fragmentation function which gives the probability for the parton to emit a photon. Because of the pointlike nature of the photon-quark interaction, it is possible to compute the leading-logarithmic behavior of the photon fragmentation function, including the corrections due to additional parton branchings. The resulting fragmentation functions are $O(\alpha/\alpha_s)$ since they possess a logarithmic growth coming from the integration mentioned above. In the leading-logarithm approximation the bremsstrahlung contribution consists of the $O(\alpha/\alpha_s)$ fragmentation functions convoluted with the various $O(\alpha_s^2)$ two-body subprocesses, resulting in a contribution of $O(\alpha\alpha_s)$. The signature of the bremsstrahlung contribution is that the photon is balanced by a jet on the opposite side of the event and it is accompanied by nearly collinear hadrons on the same side of the event.

The leading-logarithm approximation, with the corresponding collinear kinematics, gives a good qualitative description of the event structure observed in the production of high-p_T photons.[6,7] However, in order to provide a more quantitative description, it is necessary to go beyond this level of approximation. The next step in a systematic program for increasing the level of precision of the calculations would be to treat the kinematics of the $O(\alpha\alpha_s^2)$ $2\to3$ subprocesses exactly. In so doing, various collinear singularities will be encountered and a method for handling these must be employed. In addition to the three-body contributions there are one-loop corrections to the two-body subprocesses, as well. A conventional higher-order calculation of the inclusive photon cross section would proceed along the following lines. First, the singularities would be regularized using an appropriate method such as dimensional regularization.[8] The ultraviolet singularities would be subtracted after specifying a renormalization scheme such as the modified minimal-subtraction ($\overline{\text{MS}}$) scheme.[9] The collinear singularities would be factorized and absorbed into the corresponding distribution and fragmentation functions. Finally, the divergences occurring when one of the final-state partons becomes soft would be canceled by corresponding infrared singularities coming from the loop graphs. The result is a singularity-free prediction for the inclusive photon cross section. Suppose, however, that one was interested in an observable which involved simultaneously observing the photon and another particle or, perhaps, a jet. This would involve limiting the region of integration for the three-body final states. However, the collinear and soft singularities must still be treated so as to arrive at a singularity-free result. It is here that the flexibility of Monte Carlo techniques can be profitably employed. The basic idea is to partition the three-body phase space into regions which contain soft singularities, collinear singularities, or are singularity-free. The singular regions are integrated by hand in the standard fashion, thereby allowing the singularity cancellation and factorization to occur, as usual. The remaining phase-space integrations are performed using Monte Carlo techniques. In this way, one can change the calculation easily to reflect different experimental cuts, jet definitions, etc. Of course, the precise boundary between the regions where analytic or Monte Carlo integration techniques are utilized should not affect the ultimate result.

For the purpose of this section, the four-vectors of the two-body and three-body subprocesses will be labeled by $p_1+p_2\to p_3+p_4$ and $p_1+p_2\to p_3+p_4+p_5$, respectively. Lorentz scalars $s_{ij}=(p_i+p_j)^2$ and $t_{ij}=(p_i-p_j)^2$ will be used. The division of the three-body phase space into singularity-free and singular regions is implemented by the introduction of two theoretical cutoff parameters δ_s and δ_c. For the three-body subprocesses, the soft singularities are associated with the phase-space region where one final-state gluon becomes soft. The soft region is defined to be that where the relevant parton energy in the subprocess rest frame becomes less than $\delta_s\sqrt{s_{12}}/2$. If δ_s is chosen to be sufficiently small, then the relevant three-body subprocesses can be evaluated using the soft-gluon approximation wherein the the gluon energy is set to zero in the numerator of the expression. The resulting expression is then easily integrated over the soft region of phase space. At this stage, this integrated soft piece contributes to the two-body part which contains the one-loop terms. The soft and infrared singularities can then be canceled explicitly. Next, the collinear regions of phase space are defined to be those where any invariant (s_{ij}, or t_{ij}) becomes smaller in magnitude than $\delta_c s_{12}$. If δ_c is chosen sufficiently small, then in each collinear region the relevant subprocess can be evaluated using the leading-pole approximation. The result is easily integrated in n dimensions, thereby explicitly displaying the collinear singularities. These are then factorized and included in the relevant structure functions or canceled with corresponding singularities in the two-body expressions. At this point, the remainder of the three-body phase space contains no singularities and the subprocesses can be evaluated in four dimensions.

The calculation now consists of two pieces—a set of two-body contributions and a set of three-body contributions. Each set consists of finite parts, all singularities having been canceled, subtracted, or factorized. Howev-

er, each part depends separately on the two theoretical cutoffs δ_s and δ_c. Each by itself has no intrinsic meaning. In fact, for very small values of δ_s we shall see that logarithms of the cutoff will force the two-body contribution to become negative. However, when the two- and three-body contributions are combined to form a suitably inclusive observable, e.g., an inclusive single-photon invariant cross section, all dependence on the cutoffs will cancel. It will turn out that the answers are stable against variations of these cutoffs over quite a wide range. Physically, this is as it should be. The cutoffs merely serve to distinguish the regions where the phase-space integrations are done by hand from those where they are done by Monte Carlo techniques. When the results are added together, the precise location of the boundary between the two regions is not relevant. Thus, the answer becomes independent of the cutoffs. Of course, this is valid only over a certain range of cutoffs values. The cutoffs must be sufficiently small that the soft-gluon and leading-pole approximations are valid in the regions near the edge of phase space where they are used. Furthermore, when these regions are integrated over, terms which vanish in the limit of zero cutoff are discarded. This provides an additional reason for requiring small cutoffs. Finally, the cutoffs must be chosen so that the experimental cuts placed on an observable do not interfere with the cancellation referred to above. In general, this also requires small values of the cutoffs. The results reported below are stable to variations in the cutoffs, thus providing a check on the calculation. Calculating a different observable simply requires forming the appropriate histogram. This flexibility is the major advantage of the technique. The price paid for this ease of use is that two sets of Monte Carlo "events" must be generated and added together. In practice, this is not a major imposition.

From a theoretical standpoint, it is often desirable to suppress the bremsstrahlung contribution. For example, in determinations of the initial-gluon distribution one seeks to maximize the relative contribution of the $gq \to \gamma q$ subprocess. In addition, it is often necessary to apply an "isolation" cut on the electromagnetic signal in order to aid in separating the true high-p_T photon signal from signals from other sources. At the leading-log level the effect is to essentially remove the photon-fragmentation-function contribution. Alternatively, the fragmentation-function logarithm can be modified by changing the argument to one which depends on the photon-isolation angle.[10] However, an angle cut alone is not sufficient when higher-order processes are considered. Suppose, for example, that an isolated photon was defined as one which had no accompanying hadrons within a cone of half-angle δ_γ. There is the possibility that a very soft gluon could be inside the cone, but with an energy below the threshold for detection. But such soft gluons give rise to infrared singular contributions which must be treated properly in order to obtain sensible predictions. Therefore, the operational definition of an isolated photon must take this into account. One method is to define an isolated photon as one for which the associated hadronic energy in a cone of half-angle δ_γ about the photon direction is less than a fraction ϵ_h of the photon energy. This definition allows for the possibility of some soft partons accompanying the photon within the cone. To see why this is important, consider the fact that there will be some infrared singular terms from the one-loop graphs contributing to the subprocess $gq \to \gamma q$. These singularities cancel against corresponding soft singularities generated by integrating the soft gluon in the subprocess $gq \to \gamma qg$ over all of the allowed phase space. If that phase space is limited by putting an absolute veto on accompanying hadronic energy in some region of phase space, then the cancellation will be incomplete. Therefore, the modified isolation definition, which allows accompanying soft hadronic energy, must be used. Additional comments concerning the implementation of this isolation criterion are given in the Appendix.

III. RESULTS

At this point, a survey of some typical results will serve to outline the versatility and convenience of this approach. The detailed expressions utilized in the calculational scheme outlined above are given in the Appendix. For all subsequent calculations, the set-1 parton distributions of Ref. 11 will be used with $\Lambda = 200$ MeV. This corresponds to adopting the "physical" parton distribution definition wherein the distributions are defined by the deep-inelastic structure function F_2. (The set-1 parametrizations were obtained in the leading-logarithm approximation. Accordingly, only the one-loop anomalous dimensions and running coupling were used. However, for the purpose of this comparison, the results can be considered as a parametrization of the data. In addition, $\Lambda_{\overline{\rm MS}} = 200$ MeV has been used.) For the photon fragmentation functions, the parametrizations of Ref. 12 will be used. A single-scale $Q^2 \approx p_T^2$ will be used for the renormalization and factorization scales. In addition, the next-to-leading-logarithm predictions have been obtained using the two-loop expression for α_s with four flavors.

For the first example, consider the single-photon invariant cross section. In Fig. 1 the results for proton-proton collisions at $\eta_\gamma = 0$, $p_T = 6$ GeV, and $\sqrt{s} = 23$ GeV are shown versus the soft cutoff δ_s for a fixed value of the collinear cutoff δ_c. The two-body and three-body contributions are shown separately and summed. Note that as δ_s is decreased the two-body contribution becomes negative. This is a result of the explicit logarithmic dependence of the two-body part on δ_s and does not correspond to the behavior of a physical cross section. On the other hand, the three-body part shows an increase as δ_s decreases. The net result, for the sum of the two terms is constant, within the Monte Carlo statistics, over the range of δ_s shown. Figure 2 is a similar set of plots, this time as a function of δ_c with δ_s fixed. Again, the cancellation takes place, leaving a result independent of the cutoffs. This cutoff independence is a necessary, though not sufficient, check on the calculation.

The dependence of the inclusive single-photon invariant cross section on the scale Q^2 is illustrated in Fig. 3. The invariant cross section at $\eta_\gamma = 0$ is plotted for several values of p_T versus the parameter n, where both the re-

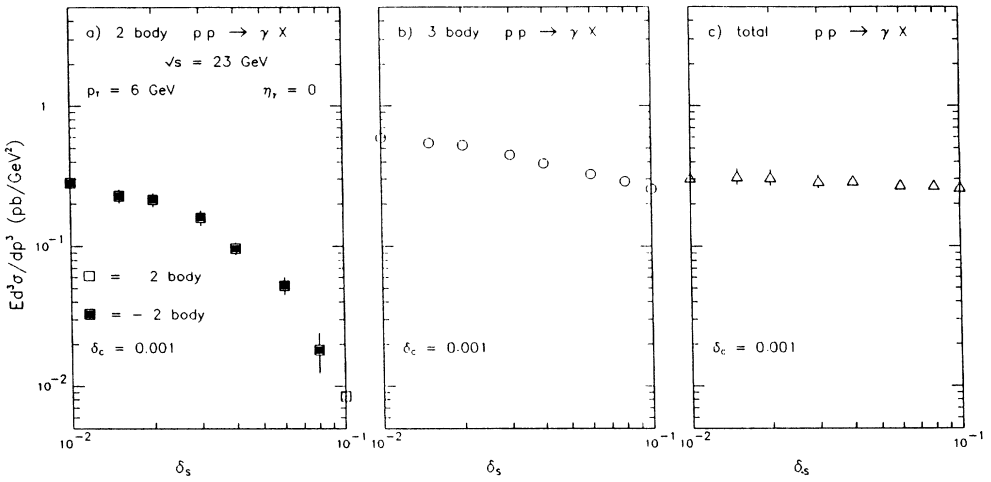

FIG. 1. The inclusive single-photon invariant cross section at $p_T(\gamma)=6$ GeV and $\eta_\gamma=0$ for pp collisions at $\sqrt{s}=23$ GeV. The two-body and three-body contributions together with their sum are shown vs the soft cutoff δ_s at $\delta_c=0.001$.

normalization and factorization scales have been parametrized as $Q^2=np_T^2$. Both the $O(\alpha\alpha_s)$ and the full $O(\alpha\alpha_s^2)$ results are shown for three values of p_T. Note that the two-loop running coupling has been used for both results, thereby providing a consistent expansion parameter so that one can judge the degree of convergence represented by the results. The $O(\alpha\alpha_s)$ result is a monotonically decreasing function of n for all values of p_T, whereas the $O(\alpha\alpha_s^2)$ result exhibits a parabolic shape which is most evident for large values of x_T ($x_T \gtrsim 0.25$), where $x_T=2p_T/\sqrt{s}$. For small values of x_T ($x_T \lesssim 0.25$) the two results are nearly parallel and the parabolic turnover of the $O(\alpha\alpha_s^2)$ result is realized only for very small values of n. On the contrary, for larger values of x_T the parabolic turnover of the $O(\alpha\alpha_s^2)$ result occurs near $n\approx 1$. This behavior is further illustrated in Figs. 4 and 5 which show results for $p\bar{p}$ collisions at $\sqrt{s}=630$ GeV and $\eta_\gamma=0$. The curves correspond to $x_T=0.064$, 0.095, 0.13, 0.51, and 0.70. The full $O(\alpha\alpha_s^2)$ results are nearly flat over the calculated Q^2 range for most of these values of x_T. The fact that the next-to-leading-logarithm results are less sensitive to variations of the scale Q^2 over a large range of x_T is one of the motivating factors for performing such a calculation. However, the sensitivity to the scale choice is still significant for small values of x_T.

Note that the ratio of next-to-leading-logarithm and leading-logarithm results is what is commonly referred to as the "K factor." Figures 3–5 show that this ratio is not just a simple multiplicative factor, but instead is in general scale dependent. The K factor also varies between different observables for the same values of Q^2, as was shown in Ref. 3. This illustrates the need for complete next-to-leading-order calculations, as opposed to approximate methods for estimating K factors, in processes involving initial-state quarks and gluons.

Next we compare the Monte Carlo results with data

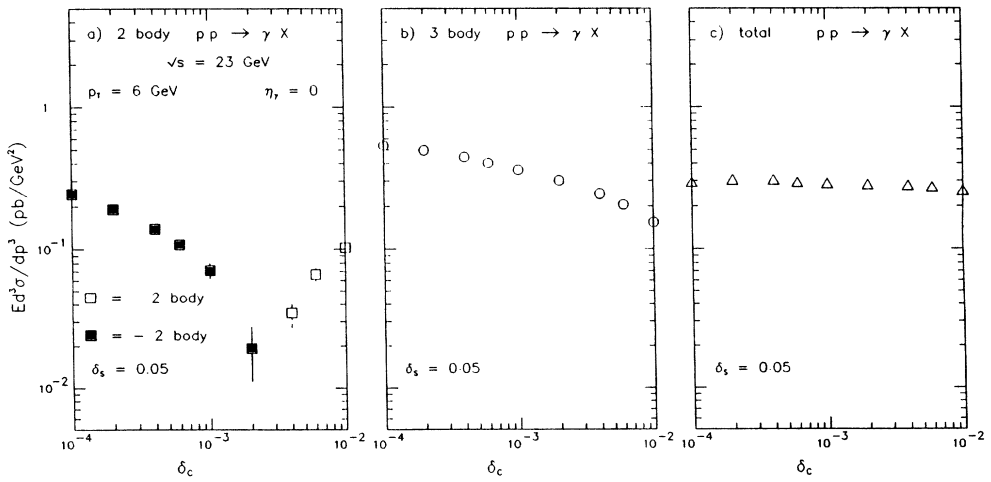

FIG. 2. Same as Fig. 1 except the results are shown vs the collinear cutoff δ_c at $\delta_s=0.05$.

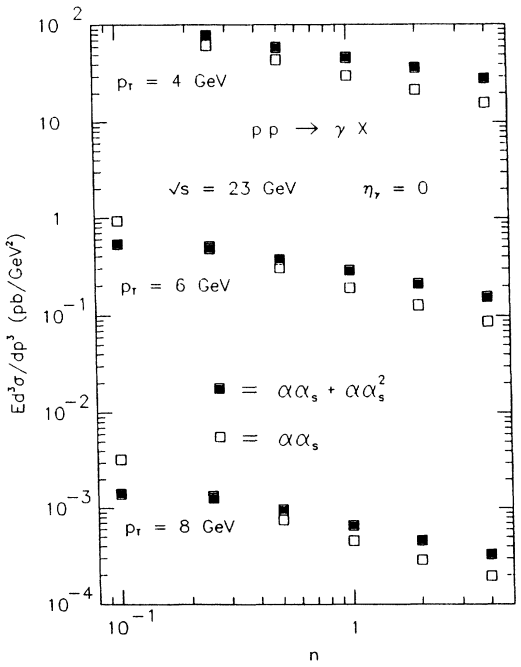

FIG. 3. The inclusive single-photon invariant cross section for pp collisions at $\sqrt{s}=23$ GeV for $\eta_\gamma=0$ and $p_T(\gamma)=4$, 6, and 8 GeV vs n, where $Q^2=np_T^2$ has been used for both the factorization and renormalization scales. Both the leading-logarithm and next-to-leading-logarithm results are shown.

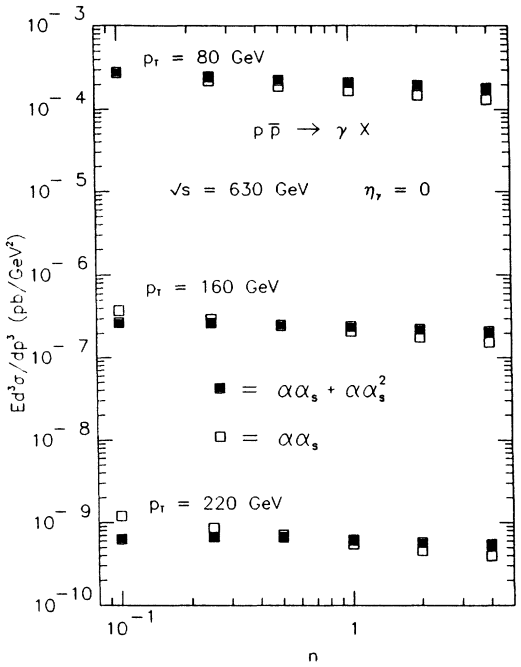

FIG. 5. Same as Fig. 3 except for $p_T(\gamma)=80$, 160, and 220 GeV.

from experiments with center-of-mass energies ranging from 23 GeV to 1.8 TeV. Some of the experiments have photon-isolation cuts whereas others do not. The photon-isolation cuts and other acceptance cuts are easily incorporated in the Monte Carlo approach illustrating the versatility and power of the method.

Figures 6 and 7 compare the next-to-leading-logarithm results for the single-photon invariant cross section at $\sqrt{s}=23$ GeV with the WA70 data of Ref. 13. Figure 6 shows the data for the invariant cross section as a func-

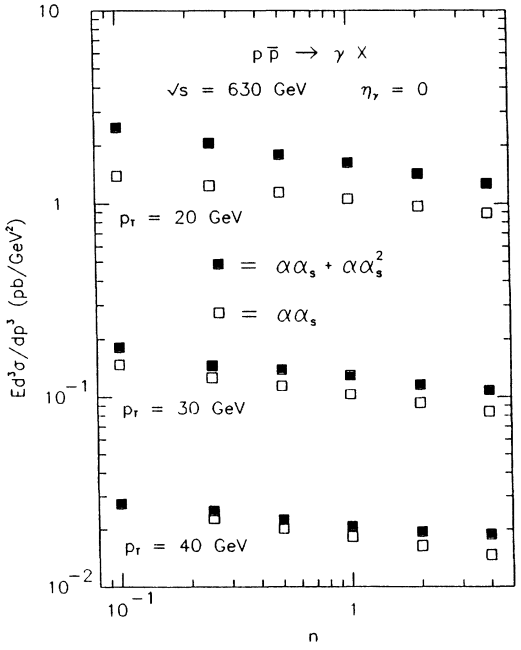

FIG. 4. Same as Fig. 3 except for $p\bar{p}$ collisions at $\sqrt{s}=630$ GeV and $p_T(\gamma)=20$, 30, and 40 GeV.

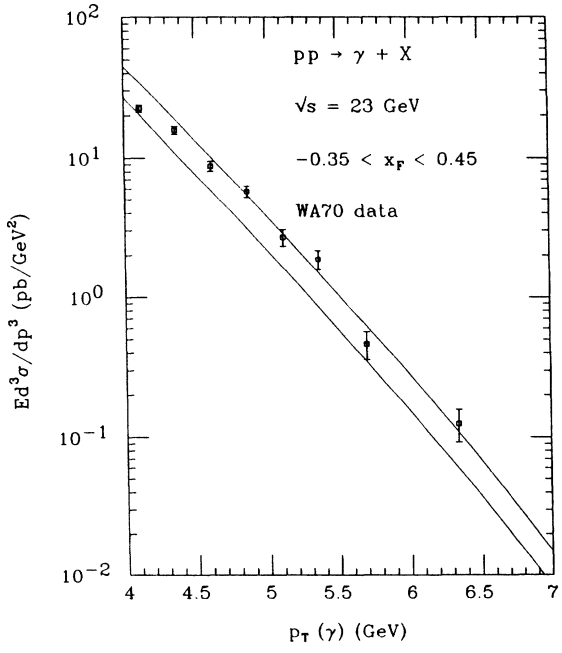

FIG. 6. Comparison between the predictions for the inclusive single-photon invariant cross section vs $p_T(\gamma)$ for $-0.35<x_F<0.45$ and the WA70 data from Ref. 13. The upper and lower curves correspond to $Q^2=\frac{1}{4}p_T^2$ and p_T^2, respectively.

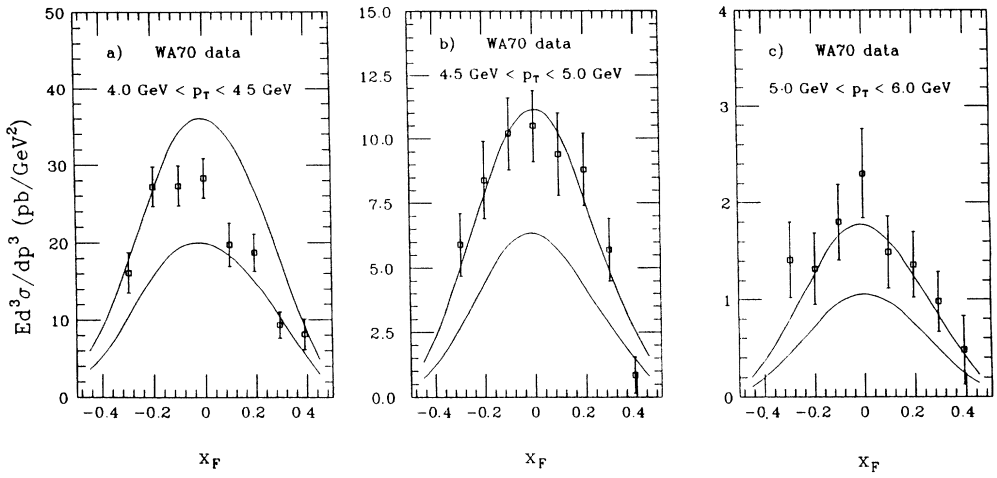

FIG. 7. Same as Fig. 6 except vs x_F. (a) 4.0 GeV $< p_T(\gamma) <$ 4.5 GeV, (b) 4.5 GeV $< p_T(\gamma) <$ 5.0 GeV, and (c) 5.0 GeV $< p_T(\gamma) <$ 6.0 GeV.

tion of $p_T(\gamma)$ for $-0.35 < x_F < 0.45$ and Fig. 7 shows the data as a function of x_F ($x_F = 2p_\parallel/\sqrt{s}$) for three p_T intervals. In both figures, the upper and lower curves correspond to $Q^2 = \frac{1}{4}p_T^2$ and p_T^2, respectively.

Figures 8 and 9 compare the next-to-leading-logarithm results for the single-photon invariant cross section at $\sqrt{s} = 630$ GeV with UA1 and UA2 data from Refs. 6 and 7, respectively. Figure 8 shows the data as a function of $p_T(\gamma)$ for $\eta_\gamma = 0$ and $\eta_\gamma = 1.4$ and Fig. 9 shows the data as a function of η_γ for three values of $p_T(\gamma)$. The pairs of curves again correspond to $Q^2 = \frac{1}{4}p_T^2$ and p_T^2. Photon-isolation cuts have been simulated by excluding any event having hadronic energy $E_H > 0.1E_\gamma$ in a cone of angle 30° about the photon momentum vector in the hadron-hadron center-of-momentum frame.

Figure 10 compares the next-to-leading-logarithm results for the single-photon invariant cross section versus p_T at $\sqrt{s} = 1.8$ TeV with the Collider Detector at Fermilab (CDF) data of Ref. 14. The two curves correspond to the Q^2 choices used in the preceding figures. It is interesting to note that the width of the band corresponding to the results for $Q^2 = \frac{1}{4}p_T^2$ and p_T^2 shrinks in size as the center-of-mass energy increases. At fixed target energies the range of x_T covered is such that the scaling violations in the parton distribution functions gives a significant decrease in the cross section as the value of n is increased, i.e., when Q^2 is increased at fixed p_T. In addition, the running coupling also decreases, thereby adding to the effect. However, at collider energies the typical values of x_T are smaller, and the scaling violations do not

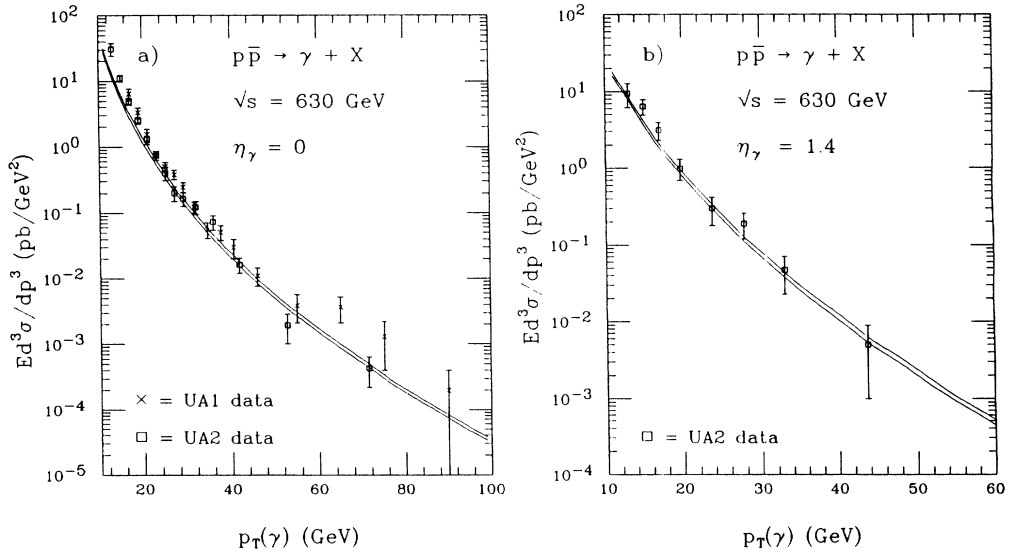

FIG. 8. Comparison between the predictions for the inclusive single-photon invariant cross section vs $p_T(\gamma)$ and the UA1 and UA2 data from Refs. 6 and 7, respectively. The upper and lower curves correspond to $Q^2 = \frac{1}{4}p_T^2$ and p_T^2, respectively. (a) $\eta_\gamma = 0$ and (b) $\eta_\gamma = 1.4$.

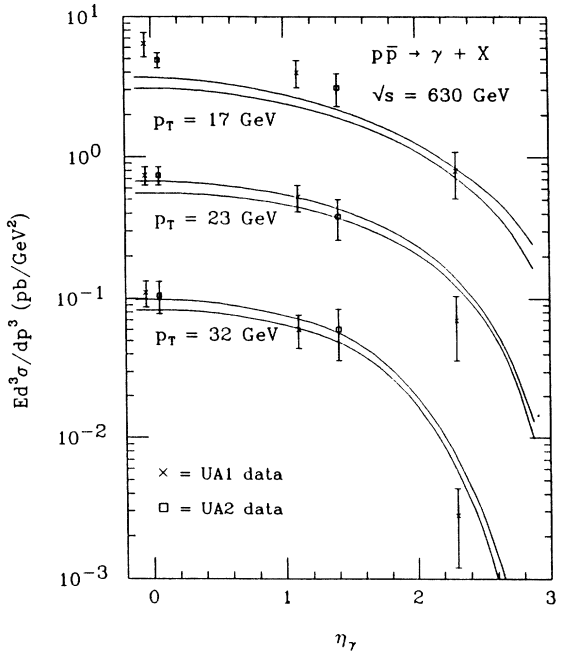

FIG. 9. Same as Fig. 8 except vs photon pseudorapidity η_γ for $p_T(\gamma)=17$, 23, and 32 GeV.

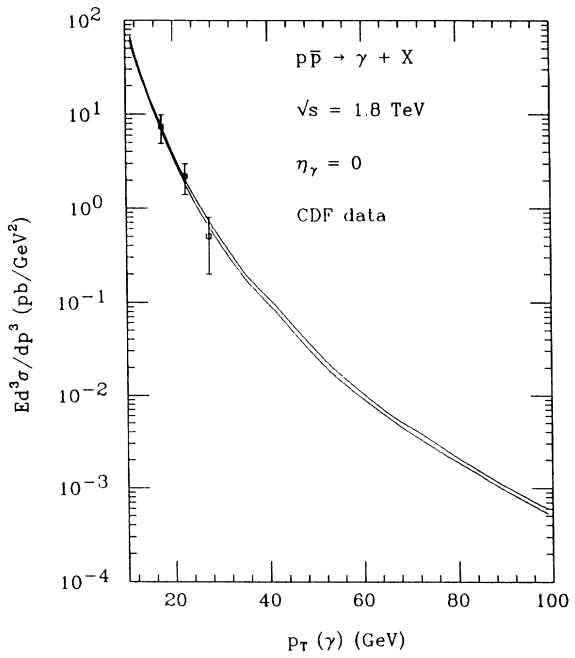

FIG. 10. Comparison between the predictions for the inclusive single-photon invariant cross section vs $p_T(\gamma)$ for $\eta_\gamma=0$ and the CDF data from Ref. 14. The upper and lower curves correspond to $Q^2=\frac{1}{4}p_T^2$ and p_T^2, respectively.

cause the parton distributions to decrease as rapidly with increasing Q^2. Indeed, for sufficiently small values of x_T, the distributions actually increase. Thus, even when the running coupling is taken into account, there is less variation with Q^2 in the small-x_T region.

The full power of the Monte Carlo method is best illustrated by considering observables which depend on correlations between the photon and another parton. For example, consider the photon-plus-jet cross section as measured by the Axial Field Spectrometer (AFS) Collaboration and presented in Ref. 15. The use of Monte Carlo integrations allows the next-to-leading-logarithm calculation of the photon-plus-jet cross section to be easily performed.[3] The inclusive photon cross-section results correspond to $|\eta_\gamma| \leq 0.7$ and they have been corrected for the effects of the isolation cut used in defining the photon

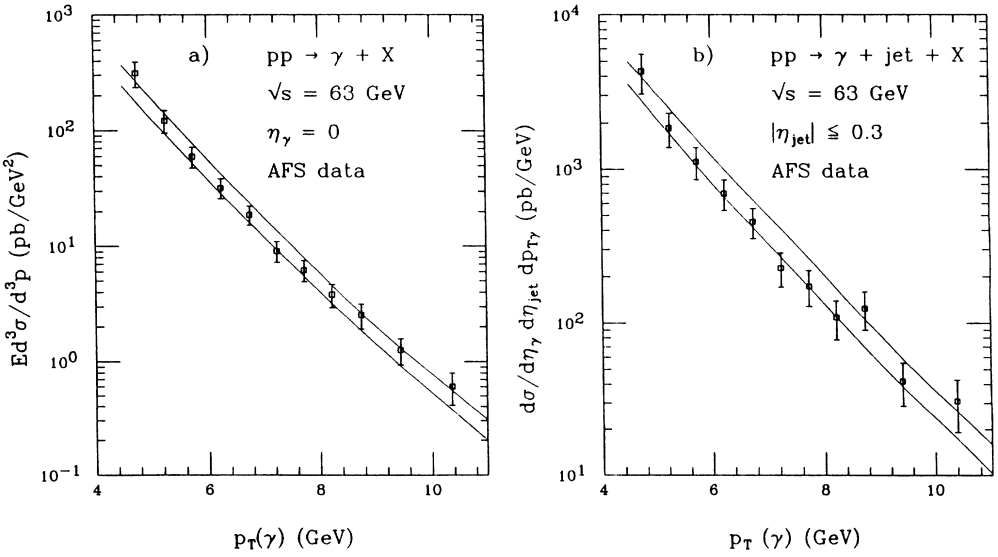

FIG. 11. Comparisons between the predictions for the single- and double-inclusive direct photon cross sections and the AFS data from Ref. 15. Part (a) is the single-inclusive photon invariant cross section at $\eta_\gamma=0$ and part (b) is the photon-plus-jet double-inclusive cross section. The upper and lower curves correspond to $Q^2=\frac{1}{4}p_T^2$ and p_T^2, respectively.

signal. Accordingly, the full bremsstrahlung contribution has been included in the calculation. The photon-plus-jet experimental results were obtained using a clustering algorithm to reconstruct the jets. The present calculation was designed to duplicate this procedure at the parton level. For the two-body contributions the requirements were simply $|\eta_\gamma| \leq 0.7$ and $|\eta_{\rm jet}| \leq 0.3$. For the three-body final states $|\eta_\gamma| \leq 0.7$ was first required. Then, partons in the region $\Delta\phi \geq 120°$ and $|\eta_{\rm jet}| \leq 0.9$ were combined to form a single jet. Here $\Delta\phi$ is the azimuthal angle between the photon and the relevant parton. Events which had a parton combination in the smaller region defined by $\Delta\phi \geq 120°$ and $|\eta_{\rm jet}| \leq 0.3$ were then used to calculate the cross section, provided that they satisfied $p_T \geq 0.3 p_{T_\gamma}$.

In Fig. 11(a) predictions for the single-photon invariant cross section are compared to the AFS data.[15] The two curves shown in Fig. 11(a) correspond to $Q^2 = \frac{1}{4}p_T^2$ (upper) and p_T^2 (lower). The band described by these two curves can be seen to yield a good description of the data.

In Fig. 11(b) predictions for the photon-plus-jet cross section $d\sigma/d\eta_\gamma d\eta_{\rm jet} dp_{T_\gamma}$ are compared to the experimental results from Ref. 15. The upper and lower curves correspond to the two choices used in Fig. 11(a). Again, the band formed by the theoretical curves coincides rather well with the experimental results. In particular, note that in neither figure was it necessary to introduce an arbitrary multiplicative K factor.

It is a straightforward procedure to calculate other types of observables, such as the away-side-jet rapidity distribution for fixed-photon rapidity and transverse momentum. Different jet definitions or photon-isolation criteria are also easily incorporated.

IV. SUMMARY AND CONCLUSIONS

Continued progress in our understanding of large-momentum-transfer processes depends on our ability to increase the level of precision of the theoretical predictions. The qualitative understanding provided by leading-logarithm calculations, while valuable, is insufficient for some purposes such as improved determinations of parton distributions and detailed tests of the underlying dynamics. Increasingly, the need for next-to-leading-logarithm calculations has become apparent. Additionally, a method for performing such calculations which possessed the capability of being adapted to differing experimental situations also became clear. With conventional analytic techniques each observable requires a new calculation and it becomes difficult to match different jets definitions, experimental cuts, etc. In this paper we have shown how a Monte Carlo–based technique can be used to develop a flexible and easy-to-use program for calculating observables with next-to-leading-logarithm accuracy in direct photon production. The methods can easily be extended to other reactions as well.

In order to demonstrate the flexibility of this technique, results for various single- and double-inclusive observables have been presented, some of which include cuts to eliminate the photon bremsstrahlung contribution in favor of the pointlike contribution. The observables are insensitive to the values chosen for the theoretical soft and collinear cutoffs used in intermediate stages of the calculation, a necessary though not sufficient constraint on the validity of the results. It has also been shown that the sensitivity to the factorization and renormalization scales depends on the observable and on the kinematic region in question. In particular, the variation with Q^2 in the region covered by available collider data is rather small.

ACKNOWLEDGMENTS

One of the authors (J.F.O.) wishes to acknowledge useful discussions concerning the definition of photon-isolation cuts with Keith Ellis.

APPENDIX

The expressions used in the next-to-leading-logarithm Monte Carlo calculation of direct photon production are summarized in this appendix. The treatment of the two-body, three-body, and bremsstrahlung contributions is given separately.

1. Two-body contributions

In this section the Mandelstam variables s, t, and u are the same as s_{12}, t_{13}, and t_{23}. In addition, it is convenient to scale t in order to obtain a variable $v = 1 + t/s$ which ranges from 0 to 1. In terms of these variables the full contribution has the form

$$\sigma_{2\ \rm body}^{\rm NLL}(AB \to \gamma + X) = \sum_q \int dv\, dx_a dx_b \left[\frac{d\bar{\sigma}}{dv}(gq \to \gamma q) + \frac{d\bar{\sigma}}{dv}(q\bar{q} \to \gamma g) + G_{g/A}(x_a, M^2) G_{q/B}(x_b, M^2) \frac{d\sigma^{\rm NLL}}{dv}(gq \to \gamma q) \right.$$
$$\left. + G_{q/A}(x_a, M^2) G_{\bar{q}/B}(x_b, M^2) \frac{d\sigma^{\rm NLL}}{dv}(q\bar{q} \to \gamma g) \right] . \quad \text{(A1)}$$

In addition to the terms shown in Eq. (A1), those with the beam and target interchanged must be included, as well. The two contributions labeled $d\sigma^{\rm NLL}/dv$ include both the two-body subprocesses calculated to $O(\alpha\alpha_s^2)$, the soft contributions from the $O(\alpha\alpha_s^2)$ three-body processes, and the contributions from the hard collinear singularities in the final state. The singularities associated with the initial-state parton distributions have been factorized and absorbed into the initial parton distributions. The terms denoted by $d\bar{\sigma}/dv$ are the remnants of the hard collinear singularities after the factorization process has been performed.

The individual terms in Eq. (A1) are

$$\frac{d\sigma^{\rm NLL}}{dv}(gq\to\gamma q)=\frac{C}{8}\alpha_s(\mu^2)T_0^{gq}+\frac{C}{8}\frac{\alpha_s^2(\mu^2)}{2\pi}(T_0^{gq}A_0+B_0)\ , \tag{A2}$$

with

$$A_0=-\tfrac{1}{6}(11N_C-2N_F)\ln\frac{s}{\mu^2}+N_C[\tfrac{1}{18}(11N_C-2N_F)+2\ln\delta_s]\ln\frac{s}{M^2}+N_C\left[4\ln^2\delta_s+\tfrac{1}{2}\ln^2\frac{-u}{s}+{\rm Li}_2\frac{-t}{s}+2\ln\delta_s\ln\frac{-u}{s}\right]$$
$$+\left[C_F-\frac{N_C}{2}\right]\left[\frac{\pi^2}{3}+4\ln^2\delta_s+\ln^2\frac{-t}{s}+\ln^2\frac{t}{u}+2{\rm Li}_2\frac{-u}{s}+4\ln\delta_s\ln\frac{-t}{s}\right]$$
$$-C_F\left[\tfrac{7}{2}+\ln^2\delta_s+(2\ln\delta_s+\tfrac{3}{2})\ln\frac{\delta_c M^2}{s}\right]+\lambda_{\rm FC}C_F\left[\frac{\pi^2}{3}+\tfrac{9}{2}+\tfrac{3}{2}\ln\delta_s-\ln^2\delta_s\right]\ ,$$

$$B_0=-\left[C_F-\frac{N_C}{2}\right]\left[\left[2+\frac{u}{s}\right]\left[\pi^2+\ln^2\frac{t}{u}\right]+\left[2+\frac{s}{u}\right]\ln^2\frac{-t}{s}+2\ln\frac{-us}{t^2}\right]-3C_F\frac{s}{u}\ln\frac{-u}{s}\ ,$$

$$T_0^{gq}=-\left[\frac{s}{u}+\frac{u}{s}\right]\ ,$$

and

$$C=\frac{2\pi\alpha}{s}e_q^2C_F\ .$$

Here δ_s and δ_c are the soft and collinear cutoff parameters introduced in Sec. II, ${\rm Li}_2(x)$ is the dilogarithm function, M^2 is the factorization scale, and μ^2 is the renormalization point. In addition, e_q is the quark fractional charge, $C_F=\frac{4}{3}$ is the quark-gluon vertex color factor, N_C is the number of colors, and N_F is the number of active quark flavors. The parameter $\lambda_{\rm FC}$ depends on the factorization convention chosen. For this calculation, $\lambda_{\rm FC}=1$ has been used, as is discussed later in this section.

The terms for $q\bar{q}\to\gamma g$ are similar:

$$\frac{d\sigma^{\rm NLL}}{dv}(q\bar{q}\to\gamma g)=\frac{C}{3}\alpha_s(\mu^2)T_0^{q\bar{q}}+\frac{C}{3}\frac{\alpha_s^2(\mu^2)}{2\pi}(T_0^{q\bar{q}}A_0+B_0)\ , \tag{A3}$$

with

$$A_0=-\tfrac{1}{6}(11N_C-2N_F)\ln\frac{s}{\mu^2}+\frac{N_F}{3}(\ln\delta_c-\tfrac{5}{3})-N_C(\tfrac{11}{6}+2\ln\delta_s)\ln\delta_c$$
$$+N_C\left[\frac{67}{18}-\frac{\pi^2}{3}+\ln^2\delta_s-2\ln\frac{-t}{s}\ln\frac{-u}{s}+2\ln\delta_s\ln\frac{ut}{s^2}\right]$$
$$+C_F\left[\ln^2\frac{-t}{s}+\ln^2\frac{-u}{s}+4\ln^2\delta_s-7+\frac{2\pi^2}{3}+(3+4\ln\delta_s)\ln\frac{s}{M^2}\right]+\lambda_{\rm FC}C_F\left[9+\frac{2\pi^2}{3}+3\ln\delta_s-2\ln^2\delta_s\right]\ ,$$

$$B_0=\left[C_F-\frac{N_C}{2}\right]\left[2\ln\frac{tu}{s^2}+\left[2+\frac{u}{t}\right]\ln^2\frac{-u}{s}+\left[2+\frac{t}{u}\right]\ln^2\frac{-t}{s}\right]+3C_F\left[\frac{t}{u}\ln\frac{-u}{s}+\frac{u}{t}\ln\frac{-t}{s}\right]\ ,$$

and

$$T_0^{g\bar{q}}=\left[\frac{t}{u}+\frac{u}{t}\right]\ .$$

The remnants of the factorization of the hard collinear singularities are given by

$$\frac{d\tilde{\sigma}}{dv}(gq\to\gamma q)=\frac{C}{8}\frac{\alpha_s^2(\mu^2)}{2\pi}T_0^{gq}\left\{G_{g/A}(x_a,M^2)\int_{x_b}^{1-\delta_s}\frac{dz}{z}\left[G_{q/B}\left[\frac{x_b}{z},M^2\right]\tilde{P}_{qq}(z)+G_{g/B}\left[\frac{x_b}{z},M^2\right]\tilde{P}_{qg}(z)\right]\right.$$
$$\left.+G_{q/B}(x_b,M^2)\int_{x_a}^{1-\delta_b}\frac{dz}{z}\left[G_{g/A}\left[\frac{x_a}{z},M^2\right]\tilde{P}_{gg}(z)+G_{q/A}\left[\frac{x_a}{z},M^2\right]\tilde{P}_{gq}(z)\right]\right\}\ , \tag{A4}$$

and

$$\frac{d\tilde{\sigma}}{dv}(q\bar{q}\to\gamma g)=\frac{C}{3}\frac{\alpha_s^2(\mu^2)}{2\pi}T_0^{q\bar{q}}\left\{G_{q/A}(x_a,M^2)\int_{x_b}^{1-\delta_s}\frac{dz}{z}\left[G_{\bar{q}/B}\left[\frac{x_b}{z},M^2\right]\tilde{P}_{qq}(z)+G_{g/B}\left[\frac{x_b}{z},M^2\right]\tilde{P}_{qg}(z)\right]\right.$$
$$\left.+G_{\bar{q}/B}(x_b,M^2)\int_{x_a}^{1-\delta_s}\frac{dz}{z}\left[G_{q/A}\left[\frac{x_a}{z},M^2\right]\tilde{P}_{qq}(z)+G_{g/A}\left[\frac{x_a}{z},M^2\right]\tilde{P}_{qg}(z)\right]\right\}, \quad \text{(A5)}$$

where

$$\tilde{P}_{ij}(z)\equiv P_{ij}(z)\ln\left[\frac{1-z}{z}\delta_c\frac{s}{M^2}\right]-P'_{ij}(z)-\lambda_{\rm FC}F_{ij}(z)\ .$$

The Altarelli-Parisi splitting functions in $4-2\epsilon$ dimensions are, for $0<z<1$,

$$P_{qq}(z,\epsilon)=C_F\left[\frac{1+z^2}{1-z}-\epsilon(1-z)\right],$$
$$P_{qg}(z,\epsilon)=\frac{1}{2(1-\epsilon)}[z^2+(1-z)^2-\epsilon],$$
$$P_{gg}(z,\epsilon)=2N_C\left[\frac{z}{1-z}+\frac{1-z}{z}+z(1-z)\right],$$
$$P_{gq}(z,\epsilon)=C_F\left[\frac{1+(1-z)^2}{z}-\epsilon z\right],$$

and can be written

$$P_{ij}(z,\epsilon)=P_{ij}(z)+\epsilon P'_{ij}(z)\ ,$$

which defines the P'_{ij} functions. The functions F_{qq} and F_{qg} depend on the choice of factorization convention. The choice $\lambda_{\rm FC}=0$ is the universal convention and $\lambda_{\rm FC}=1$ is the physical convention. We adopt the physical convention and use

$$F_{qq}(z)\doteq C_F\left[\frac{1+z^2}{1-z}\ln\left[\frac{1-z}{z}\right]-\frac{3}{2}\frac{1}{1-z}+2z+3\right],$$
$$F_{qg}(z)=[z^2+(1-z)^2]\ln\left[\frac{1-z}{z}\right]+8z(1-z)-1\ .$$

The functions F_{gg} and F_{gq} are not uniquely determined in deep-inelastic scattering; we set them to zero, although other choices are possible.[16]

2. Three-body contributions

The cross section for this contribution is

$$\sigma_{3\ \rm body}(AB\to\gamma+X)$$
$$=\sum_{abcd}\int G_{a/A}(x_a,M^2)G_{b/B}(x_b,M^2)$$
$$\times d\hat{\sigma}(ab\to\gamma cd)dx_a dx_b\ .$$

The squared matrix elements for the $2\to3$ photoproduction subprocesses can be found in Refs. 5 and 17. The integration over three-body phase space and $dx_a dx_b$ is done numerically by standard Monte Carlo techniques. The kinematic invariants s_{ij} and t_{ij} are first tested for soft and collinear singularities. If an invariant for a subprocess falls in a soft or collinear region of phase space, the contribution from that subprocess is not included in the cross section.

3. Photon-bremsstrahlung contributions.

The photon-bremsstrahlung contribution to direct photon production is calculated by convoluting the $2\to2$ QCD subprocesses with the photon fragmentation function and the appropriate parton distribution functions:

$$\sigma_{\rm brem}=\sum_{abcd}\int G_{a/A}(x_a,M^2)$$
$$\times G_{b/B}(x_b,M^2)D_{\gamma/c}(z,M_f^2)$$
$$\times\frac{d\hat{\sigma}}{dv}(ab\to cd)dx_a dx_b dz\,dv\ .$$

The squared matrix elements for the $2\to2$ QCD subprocesses can be found in Ref. 1.

At the next-to-leading-log level there are collinear singularities associated with final-state bremsstrahlung which must be factorized and absorbed into fragmentation functions. This will modify the leading-log quark fragmentation functions as

$$D^{\rm NLL}_{\gamma/q}(z)=D^{\rm LL}_{\gamma/q}(z)$$
$$+\frac{\alpha}{2\pi}\left[P_{\gamma q}(z)\ln\left[z(1-z)\delta_c\frac{\hat{s}}{M^2}\right]-P'_{\gamma q}(z)\right]$$

(the gluon fragmentation function is unchanged). The new term is the remnant of the collinear singularity after the factorization process has been performed. If a photon-isolation cut of the type discussed in Sec. II is included, then the range of z is reduced to $1/(1+\epsilon_h)\le z\le1$. For the leading-log fragmentation functions we use the following parametrizations from Ref. 12:

$$zD^{\rm LL}_{\gamma/q}(z,Q^2)=F\left[\frac{e_q^2(2.21-1.28z+1.29z^2)z^{0.049}}{1-1.63\ln(1-z)}\right.$$
$$\left.+0.0020(1-z)^{2.0}z^{-1.54}\right],$$
$$zD^{\rm LL}_{\gamma/g}(z,Q^2)=\frac{0.194}{8}F(1-z)^{1.03}z^{-0.97},$$

where $F=(\alpha/2\pi)\ln(Q^2/\Lambda^2)$ and $\Lambda=200$ MeV. The functions $P_{\gamma q}(z)$ and $P'_{\gamma q}(z)$ are given by the functions $P_{gq}(z)$ and $P'_{gq}(z)$ with C_F replaced by e_q^2.

[1]J. F. Owens, Rev. Mod. Phys. **59**, 465 (1987).
[2]L. Cormell and J. F. Owens, Phys. Rev. D **22**, 1609 (1980); E. Berger, E. Braaten, and R. Field, Nucl. Phys. **B239**, 52 (1984).
[3]H. Baer, J. Ohnemus, and J. F. Owens, Phys. Lett. B **234**, 127 (1990).
[4]H. Baer, J. Ohnemus, and J. F. Owens, Phys. Rev. D **40**, 2844 (1989).
[5]P. Aurenche, R. Baier, A. Douiri, M. Fontannaz, and D. Schiff, Nucl. Phys. **B286**, 553 (1987).
[6]UA1 Collaboration, C. Albajar *et al.*, Phys. Lett. B **209**, 385 (1988).
[7]UA2 Collaboration, R. Ansari *et al.*, Z. Phys. C **41**, 395 (1988).
[8]G. 't Hooft and M. Veltman, Nucl. Phys. **B44**, 189 (1972).
[9]W. A. Bardeen, A. J. Buras, D. W. Duke, and T. Muta, Phys. Rev. D **18**, 3998 (1978).
[10]P. Aurenche, R. Baier, and M. Fontannaz, Report No. Fermilab-PUB-89/226-T (unpublished).
[11]D. W. Duke and J. F. Owens, Phys. Rev. D **30**, 49 (1984).
[12]D. W. Duke and J. F. Owens, Phys. Rev. D **26**, 1600 (1982).
[13]WA70 Collaboration, M. Bonesini *et al.*, Z. Phys. C **38**, 371 (1988).
[14]Collider Detector at Fermilab (CDF) Collaboration, R. Blair *et al.*, Report No. ANL-HEP-CP-89-07, 1989 (unpublished).
[15]Axial Field Spectrometer (AFS) Collaboration, T. Åkesson *et al.*, Report No. CERN-EP/89-98, 1989 (unpublished).
[16]R. K. Ellis and J. C. Sexton, Nucl. Phys. **B269**, 445 (1986).
[17]The expressions in Ref. 5 for the $qq \to qq\gamma$ and $qq' \to qq'\gamma$ subprocesses contain a number of typographical errors where the variable a_3 appears in place of a_5. The original report, LPTHE Orsay 86/24, contains the correct expressions.